Symposium on Materials Science

Mátraháza, Hungary, October 5-7, 2022

Editor:
Miklós Fried
Department of Microelectronics and Technology, Óbuda University
2023

Organizing and Programme Committee:

Miklós Fried (editor, Department of Microelectronics and Technology, Óbuda University)

Ákos Nemcsics (Department of Microelectronics and Technology, Óbuda University)

Attila Bonyár (Department of Materials Science and Engineering, Budapest University of Technology and Economics)
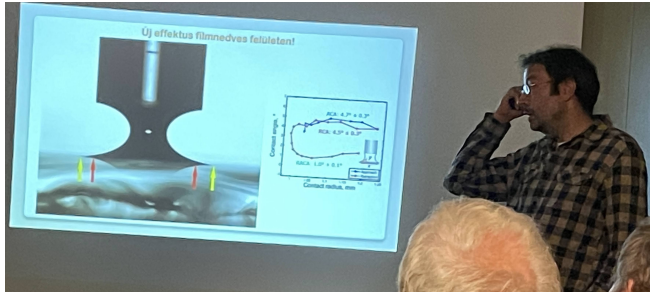
Péter Petrik (Institute of Technical Physics and Material Science, Centre for Energy Research)

András Deák (Institute of Technical Physics and Material Science, Centre for Energy Research)

Table of contents

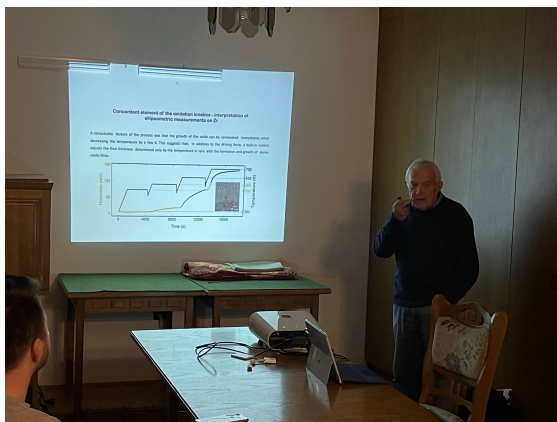Lecturers: Norbert Nagy

Dániel Péter Szekrényes

Lecturers: Ákos Nemcsics

György Sáfrán

Lecturers: Miklós Serényi

Miklós Fried

Lecturers: Ákos Nemcsics

András Deák

Lecturers: Dániel Zámbó

Péter Petrik

Lecturers: Benjamin Kalas

Alekszej Romanenko

Lecturers: József Bálint Renkó   Attila Bonyár

The Symposium

Combinatorial Preparation and Characterization Methods for High Throughput Study of WO₃-MoO₃ Mixtures

Noor Taha Ismaeel[1,2], Zoltán Lábadi[2], Miklós Fried[1,2]

[1]Institute of Microelectronics and Technology, Obuda University, Tavaszmezo Str. 17, Budapest 1084, Hungary
[2]Institute of Technical Physics & Materials Science, Centre for Energy Research, Konkoly-Thege Rd. 29-33, Budapest 1121, Hungary
*E-mail address: fried.miklos@uni-obuda.hu

The physical, chemical and structural properties of the cutting-edge materials are strongly dependent on their composition. The common procedure to reveal the properties of concentration dependent phases is the preparation of numerous two (or more)-component samples, one for each C(a)/C(b=1-a) composition, and the investigation of these individuals. This is a low efficiency procedure that costs enormous time of man and machine. Contrarily, using the combinatorial material synthesis approach, materials libraries can be produced in one experiment that contain up to several hundreds or thousands of samples on a single substrate. In order to identify optimized material structures in an efficient way, adequate automated micro-spot material characterization tools have to be applied. These methods can help us to search more efficient advanced functional materials for micro-, nano- and optoelectronics, energy converters (solar cells) or different (optical or gas) sensor systems.

Fig. 1 Measured and fitted spectra at one sample point: 2-Tauc-Lorentz (2-T-L) oscillator model. (a) Fit error (MSE) = 29.2, Thickness = 230.4 ± 0.8 nm, Amp1 = 58.0 ± 1.5, Amp2 = 11.4 ± 0.7, and Effective Medium Approximation model; (b) fit error (MSE) = 24.8, Thickness = 218.0 ± 0.1 nm, EMA% (Mat2) = 28.5 ± 1.3.

Herein, we compare the "goodness" of different optical models depending upon the sample preparation conditions, for instance, the speed and cycle number of the substrate motion. Finally, we can choose between appropriate optical models (2-Tauc-Lorentz oscillator model vs. the Bruggeman Effective Medium Approximation, BEMA) depending on the process parameters. If one has more than one "molecular layer" in the "sublayers", BEMA can be used, see Fig. 1. If one has an atomic mixture, the multiple oscillator model is better (more precise) for this type of layer structure, see Fig. 2. [M. Fried et al: *Investigation of Combinatorial WO3-MoO3 Mixed Layers by Spectroscopic Ellipsometry using Different Optical Models*, Nanomaterials 2022, 12(14), 2421]
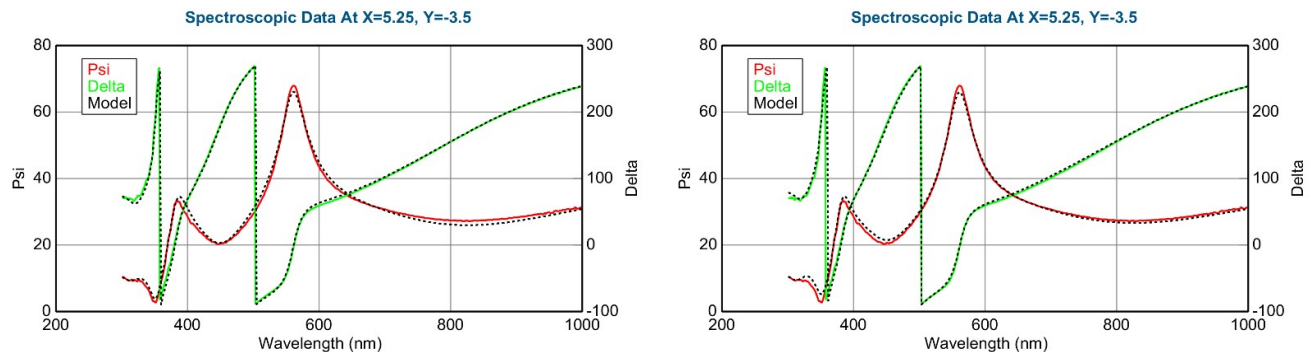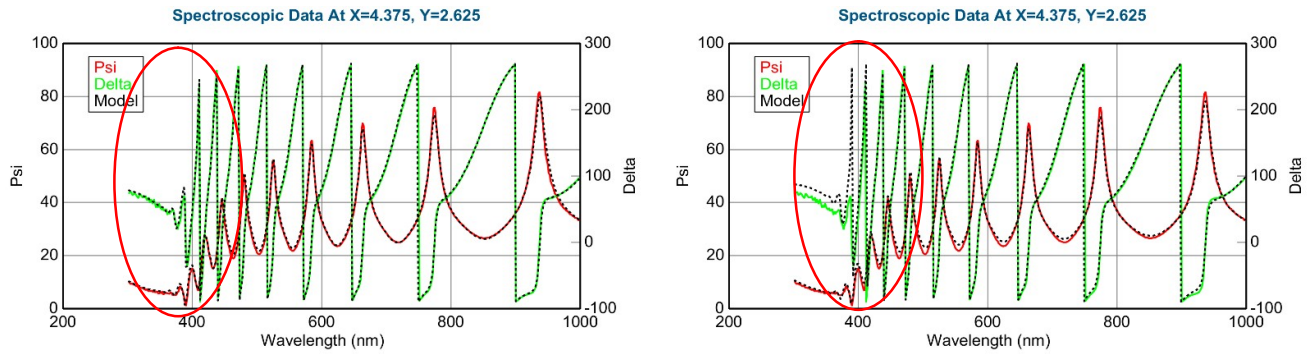
Fig. 2 Measured and fitted spectra at one sample point: 2-Tauc-Lorentz (2-T-L) oscillator model. (a) Fit error (MSE) = 30.4, Thickness = 1159.6 ± 2.9 nm, Amp1 = 39.2 ± 1.1, Amp2 = 26.7 ± 0.4), and Effective Medium Approximation model; (b) fit error (MSE) = 40.1, Thickness = 1081.7 ± 2.8 nm, EMA% (Mat2) = 41.8 ± 0.8).

We are able to map big area (30x30 cm) samples in relatively low time (Fig. 3 a) and we can control our optical method by independent measuring method, see Fig. 3 b and c.
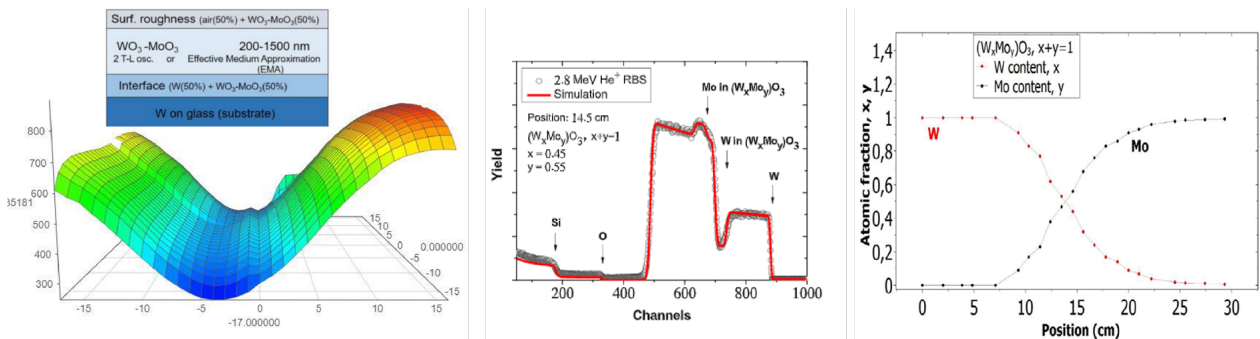
Fig. 3 a., Ellipsometric thickness mapping of the combinatorial layer b., One Rutherford Backscattering Spectrometry example near the centre position. c., Composition-map along a line by Rutherford Backscattering Spectrometry

Using this method, we are able to determine the thickness and composition map of the samples prepared for electrochromic measurements, see Fig. 4 and 5. We used the Si-pieces for control. The glass samples are for the electrochromic measurements with an ITO (transparent, conductive layer) between the glass and the investigated layer. We publish the results of the electrochromic measurements in the near future.

Fig. 4 The Si-probe (center part of upper-left photograph)
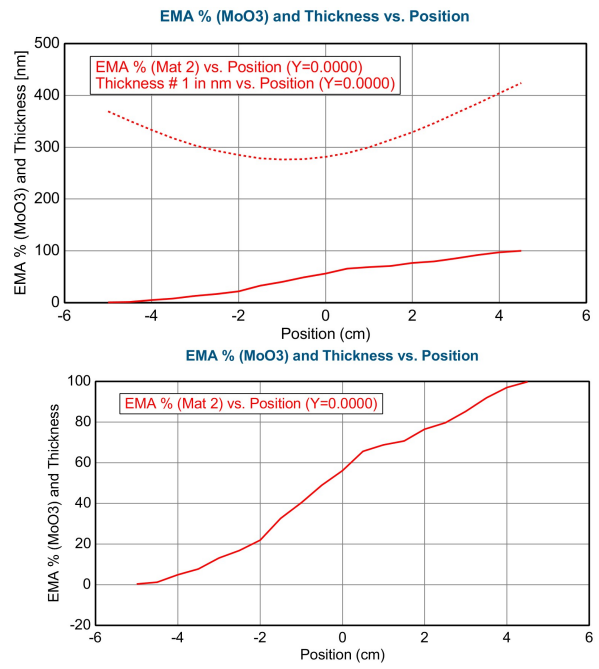
Fig. 5 Results of the control spectroscopic ellipsometric measurements on the Si-probe

Capillary Bridge Probe method on hydrophobic surfaces: liquid bridges without neck or haunch

N. Nagy[1*]

[1]*Institute of Technical Physics and Materials Science, Centre for Energy Research, P.O. Box 49, H-1525 Budapest, Hungary*

The developed indirect Capillary Bridge Probe method combines the accuracy of the Wilhelmy method and the general usability of the sessile drop method without their limitations. The method is based on the use of a liquid bridge as a probe: the capillary bridge of the test liquid is stretched between the base of a cylinder and the investigated surface under equilibrium conditions. The advancing contact angle on the sample can be measured during the slow (quasi-static) decrease of the bridge length. The receding contact angle is determined during the retraction of the cylinder. The contact angle is calculated from Delaunay's analytical solution, while the three necessary parameters are the measured capillary force (F_c), the radius of neck or haunch (r_0), and the radius of the contact line (r_s) on the investigated surface. The latter two parameters are obtained from the automated analysis of the captured image of the liquid bridge. The radius of the upper contact line (r_c) is constant since it pins on the rim of the cylinder.

The evaluation of full measurement cycles on hydrophobic surfaces is difficult, because several measured state of a water liquid bridge e.g. on a PTFE surface do not contain the neck or haunch region, as it is shown in Fig. 1. Therefore, one necessary parameter, the neck/haunch radius is unknown. How can be these measurements evaluated?
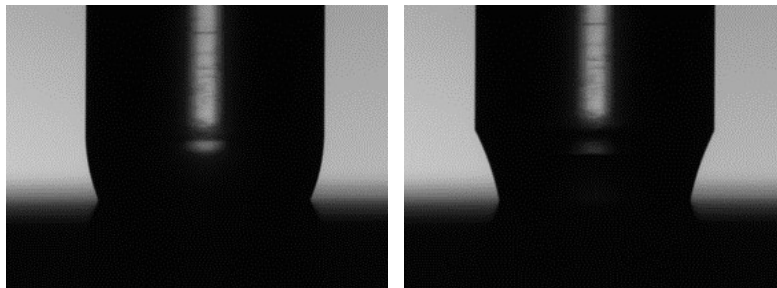
Figure 1. *Water liquid bridges without the haunch (left) and the neck (right) region, captured on a PTFE surface.*

Four different subcases can be identified to solve this problem: neck or haunch is missing and the upper or the lower part of the bridge is observable. These four cases can be seen in Fig. 2.
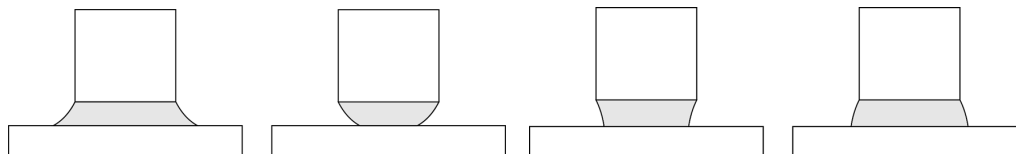
Figure 2. *Four different subcases of capillary bridges without neck or haunch.*

The two schematics to the left represent the lower part, while the two other show upper part of a liquid bridge. If we see the lower part, the surface radius (rs) can be measured. Let's complete the shape of the bridge with the missing part so that let the upper contact radius match the radius of the cylinder (see Fig. 3)! The resulted liquid bridge has the same radius, curvature, and capillary force as the real one has because of the constant mean curvature of the Plateau-surfaces. Polynomial fitting of the contour results an estimated contact angle on the investigated surface by derivation. According to this value, a contact angle range can be defined, thereby the potential liquid bridges can be found in the previously calculated look-up tables! Finally, the most appropriate capillary bridge with one

definite r0 is chosen according to the position of the lower contact points. Therefore, all parameters (including volume and surface area) can be calculated analytically.
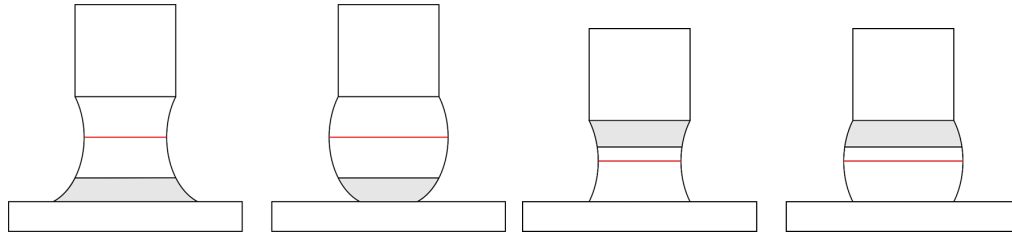
***Figure 3.** Completing the shape of capillary bridges with the missing part.*

In those cases when the the upper part appears, the problem seems to be more complicated because the surface radius is also unkown. In this situation, the solution is to find a symmetric liquid bridge, i.e. where the surface radius is equal to the radius of the cylinder! The capillary force of the completed bridge is identical to the force of the real liquid bridge due to their constant mean curvature. Due to the symmetry, the contact angle on the rim of the cylinder is equal to that which is formed on the imaginary surface. From this point, the procedure is similar to the previous cases: the polynomial fit helps to find a contact angle range and the position of the (real) contact points chooses the right nech/haunch radius of the capillary bridge. Now, we have all three input parameters to calculate every parameter of the real, original liquid bridge: contact angle on the sample surface, length, volume, area, etc.

A water liquid bridge streched between the cylinder and a Zeonex-coated surface forms all of the four different subcases during one measurement cycle. Fig. 4 shows evaluated examples of these equlibrium states. The order of images in Fig. 4 follows the previous order of different subcases, not the measured sequence.
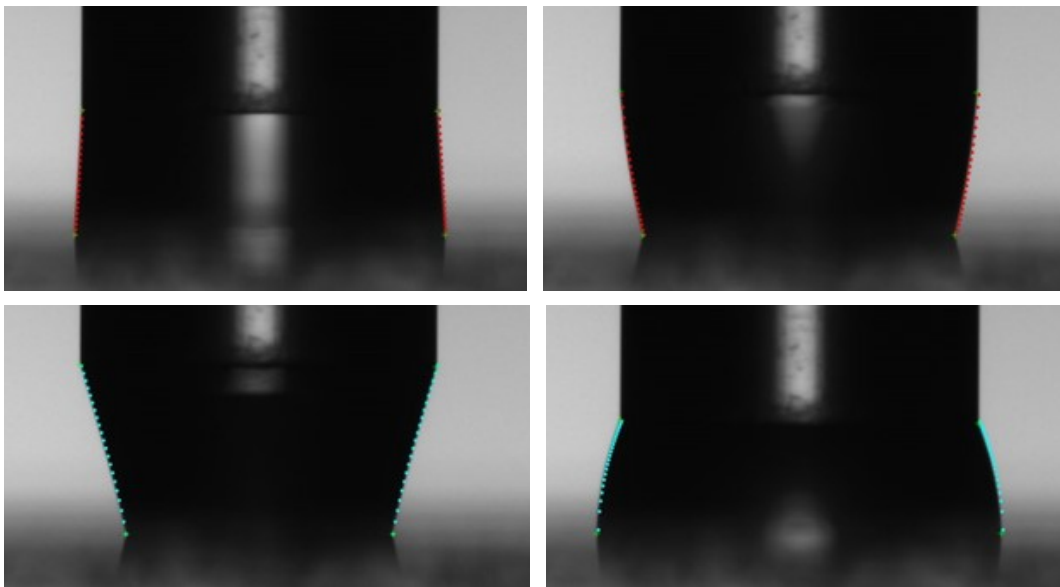
***Figure 4.** Evaluated images of a water capillary bridge formed on a Zeonex-coated surface during one measurement cycle. The order of images follows the previous order of different subcases, not the measured sequence.*

References

[1] N. Nagy: Capillary Bridges on Hydrophobic Surfaces: Analytical Contact Angle Determination, *Langmuir* **38**, 2022, 6201-6208

Multi-color ellipsometric mapping tool from cheap parts

Berhane Nugusse[1,2], György Juhász[1], Csaba Major[1], Péter Petrik[1], Sándor Kálvin[1], Zoltán György Horváth[3], Miklós Fried[1,2*]

[1]Institute of Technical Physics and Materials Science, Centre for Energy Research, Konkoly-Thege Rd. 29-33, Budapest 1121, Hungary
[2]Institute of Microelectronics and Technology, Obuda University, Tavaszmezo Str. 17, Budapest 1084, Hungary
[3]Institute for Solid State Physics and Optics, Wigner Research Centre for Physics, Konkoly-Thege Rd. 29-33, Budapest 1121, Hungary
*E-mail address: fired.miklos@ek-cer.hu

Non-destructive techniques are important methods to use during all stages of the thin film processes. Spectroscopic Ellipsometry (SE) is one of such methods.

SE is a non-destructive, noninvasive and non-intrusive optical technique. It is a technique that measures the change in polarization state of the measurement beam induced by reflection from or transmission though the sample. Ellipsometry measures the amplitude ratio (tan ψ) and phase difference (Δ) between the parallel (p) and normal (s) polarizations. During data analysis, information about the system under the study is obtained by fitting measured ellipsometric spectra to optical and structural models, as ellipsometry does not give a direct information of the sample in consideration.

Generally, the aim of this research is to make a prototype optical mapping tool for materials using only cheap parts such as a tablet, monitor, big screen TV (LCD or LED) and a pinhole camera. Our arrangement shows similarity to the solution of Bakker et al, using a computer screen as a light source and a webcam as a detector in an imaging off-null ellipsometer. [10]

The basis of the work is a patent from our Institute: Horváth Z Gy, Juhász G, Fried M, Major C, Petrik P: Imaging optical inspection device with a pinhole camera; EP2160591B1, Submission Number: PCT/HU2008/000058, NSZO: G01N21/8422, Country of patent: Europe. [1-9]

The new concept of the non-collimated beam ellipsometer prototype is set up as shown in Fig. 1. A LED-LCD monitor (or a TV), see Fig. 1 a) (C) serves the polarized RGB colored light (see the built-in polarizer sheet, number 4 in Fig. 1 b) and a polarization sensitive camera behind a pinhole (7&8) together. The LCD monitor (Dell UltraSharp™ U2412M, GB-LED) is used in a 45-degree rotated position, measured by a digital angle gauge with 0.1 deg precision. In straight-through position, we can detect the extinction of the polarization sensitive camera better than 10^{-2}.

The polarization sensitive camera sensor (The Imaging Source Company's DYK 33UX250 USB 3.0 Polarsens camera), see in Fig. 1 a) (A) and in Fig. 2, serves the polarization state data, from 0, 45, 90, 135-degree rotation positions (plus 3 RGB colors in each position). This arrangement is equal to a conventional static photometric rotating analyzer ellipsometer [11, 12].

The sample is illuminated by a non-collimated light through a fixed polarizer at an azimuth of 45 degrees to the plane of incidence. The reflected light passes through a virtual "rotating analyzer" and the intensity is captured by a two-dimensional position sensitive photodetector system at four different angular positions of the analyzer.

Minimum 3 different analyzer positions are required. These four polarization states (intensity) data (at 0, 45, 90, 135-degree rotation positions) are enough (the fourth date is good to reduce the error) to determine the ellipsometric angles: ψ and Δ. Our camera serves the data for 3 colors, so we have 3x2 measured ψ and Δ.

Schematic structure of a 2/3 inch Sony CMOS Pregius Polarsens sensor (IMX250MZR) is shown in Fig. 2 b) and c). The main advantage of the assembly is that no moving parts in the system!
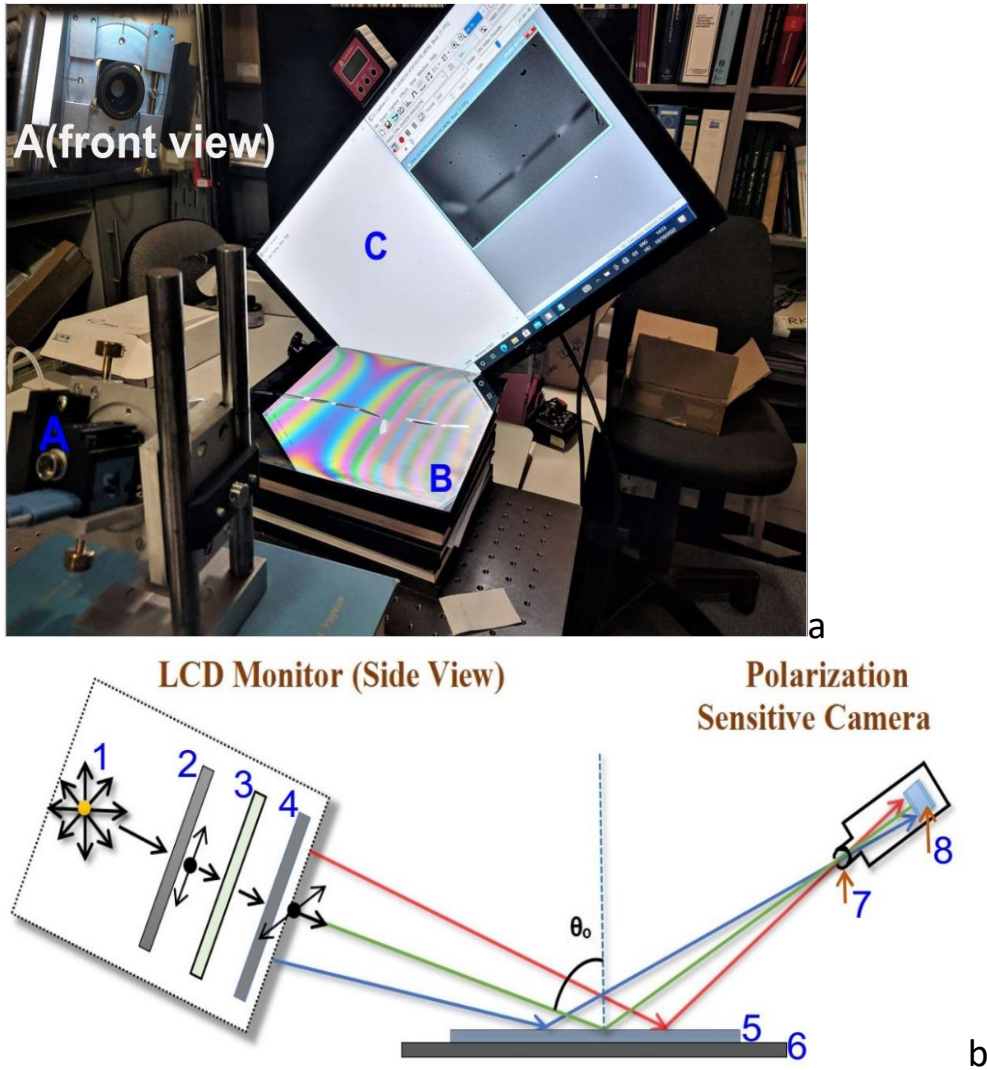
Fig. 1 (a) Experimental set-up: A) Polarization sensitive camera B) Sample + Sample holder C) LCD monitor rotated into 45° position – Upper-left: the pinhole in front of the camera

   (b) Schematics of the non-collimated beam ellipsometer: 1) Light source 2) Vertical polarizer 3) Liquid crystal cell 4) Horizontal polarizer - (C) 5) Sample - (B) 6) Sample holder 7) Pinhole (sub-mm size) 8) Camera sensor (A)
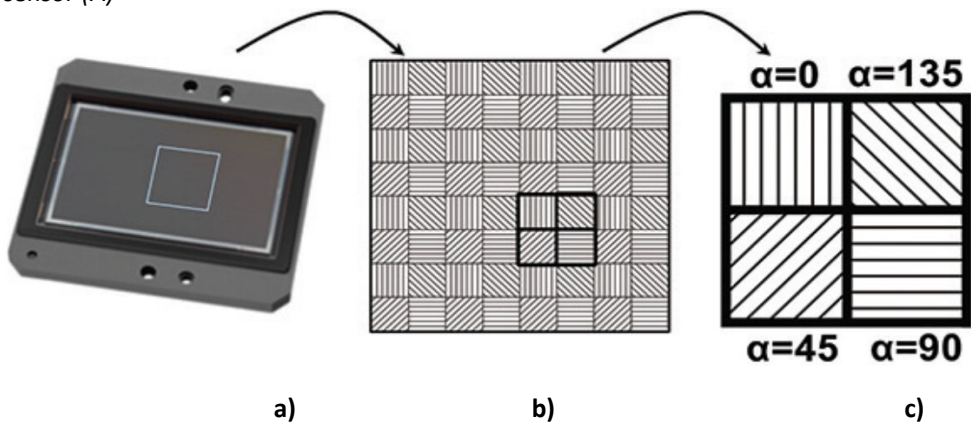
Fig. 2 Schematic structure of a 2/3 inch Sony CMOS Pregius Polarsens sensor (IMX250MZR) a). Camera sensor b). Polarizer array matched to detector pixels c). Unit cell (Super pixell)

We used a Woollam M-2000DI Rotating Compensator Spectroscopic Ellipsometer as a control measuring device. The M2000 SE system with the CompleteEASE software is used to serve the optical properties, layer thicknesses and other related parameters of the sample.

In principle, as the angle of incidence varies along the surface, we used a point-by-point angle of incidence calibration (see Fig. 1 b) using a well-known silicon-dioxide-silicon (SiO2/Si) sample. Each pixel-group (30x50 pixel-groups instead of several millions pixels) gets a calibrated angle value. If we know the refractive indices, only the angle of incidence and the actual thickness of the SiO2 layer are the unknown parameters. This way, we can calculate them from the measured ellipsometric parameters.
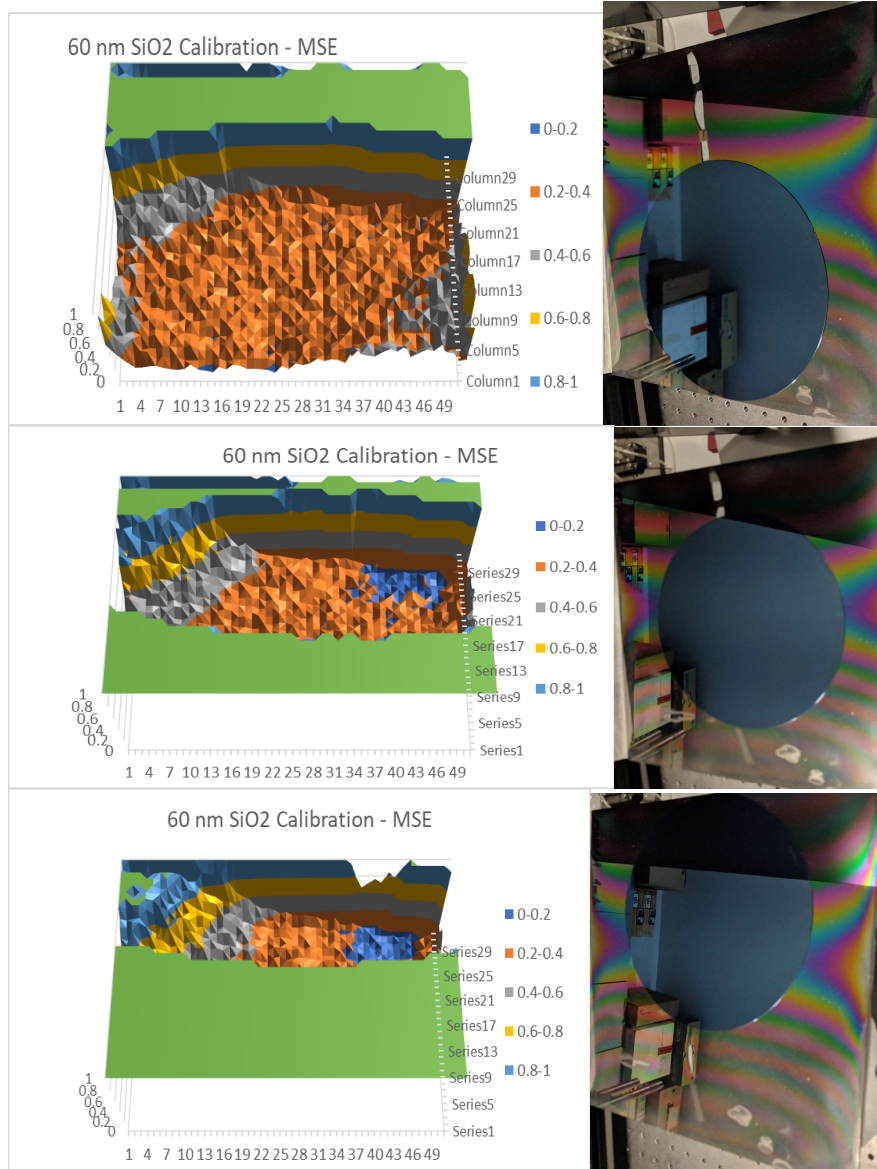
Fig. 3 The Mean Squared Error (MSE) maps of the 20 cm diameter SiO2 samples in the case of different positions. The higher MSE values show the areas, where no sample.

We used a 20 cm diameter, nominally 60 nm thick SiO2/Si sample to determine the angle of incidence point-by-point. We put the sample different positions (see the photos in Fig. 3) and one can see the "good" areas from the Mean Squared Error (MSE) maps.

The second step was choosing the points of lowest MSE values from the experimental results of these three different positions and developing corresponding single map calibration of the MSE and actual angle of incidence calibration for each coordinates. The results are shown in Fig. 4 below.
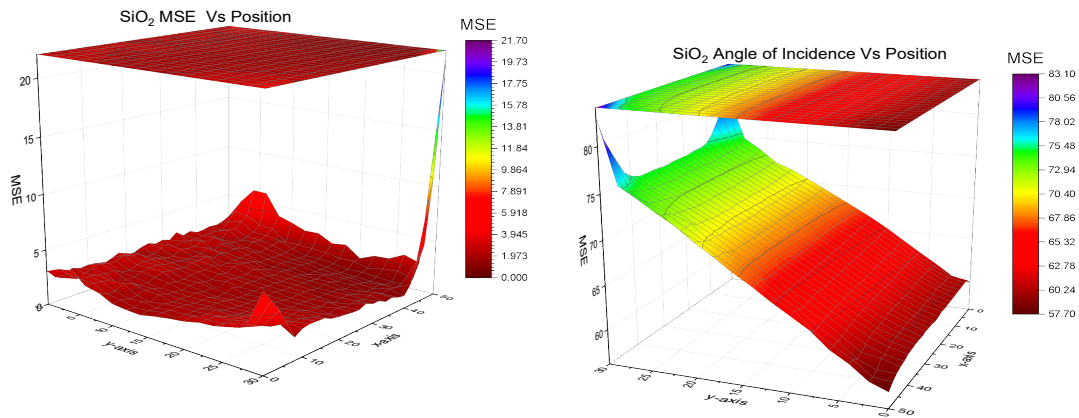
Fig. 4 MSE and corresponding angle of incidence calibration for each coordinates, respectively.

Our M2000 ellipsometer can map only 15 cm diameter area in one cycle, while the "Cheap" imaging tool assembly maps bigger area than the actual size of the measured Si-wafer, see Fig. 3. The interesting part is only the central part of the map, a region that shows the thickness of the sample, about 60-61 nm, which is close to the other (to the left) map from the conventional M2000 ellipsometer. The two scales are shifted by 2.5 nm. Determined thickness differences between "Cheap" imaging tool and M2000 measurements are about 2 nm, see Fig. 5.
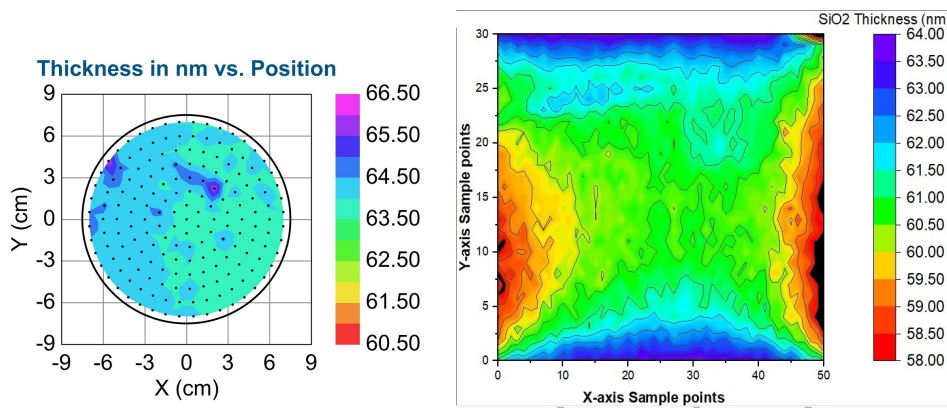
Fig. 5 Determined thickness maps from M2000 ellipsometer (left) and the corresponding measurements from the "Cheap" imaging tool assembly (right). The two scale are shifted by 2.5 nm

We measured a little bit more complex poly-Si-on-SiO2 samples. These poly-Si-on-SiO2 layers were on top of 6-inches Si-wafers. We used the previously calibrated angle-of-incidence values. Fig. 6 and 7 shows the results. The low MSE values show the samples. We must note that the perspective shortening makes worse the upper part. We show the thickness map of the "lower" part in Fig. 7. We compare the results with the M2000 results, too.
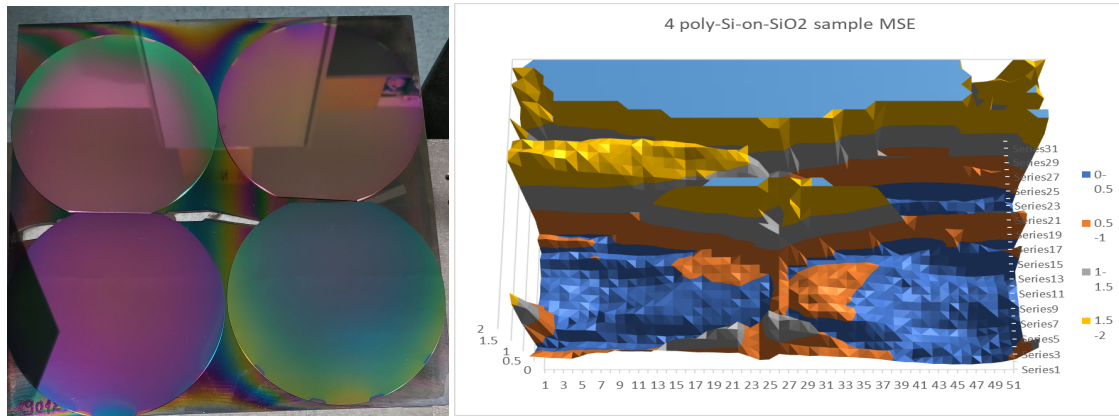
Fig. 6 Photograph of the poly-Si-on-SiO2 samples on 6-inches Si-wafers (left) and MSE-map (right),
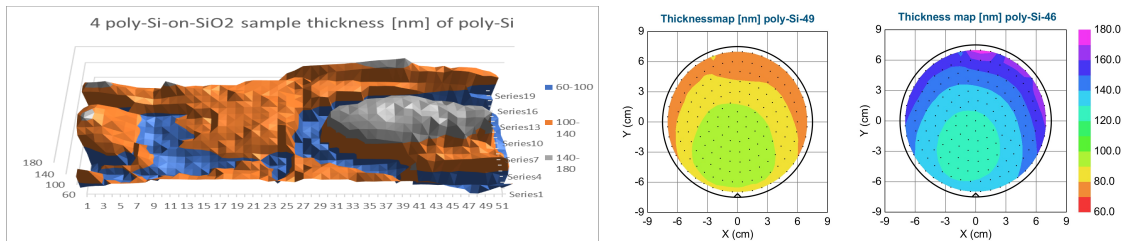
Fig. 7 Thickness maps of poly-Si samples by "Cheap" ellipsometer (left) and by M2000 (right)

We must note that three colors (wide wavelength bands) are in action, which limits the precision. Besides, there is a '0.1 degree' angle uncertainty from the digital angle gauge used in rotation angle of the LCD monitor which may be estimated to contribute to the experimental result deviation from the nominal value, as the incident polarization state of the light is determined by the rotation angle of the monitor.

Acknowledgements

References

[1] Horváth, Z Gy; Juhász, G; Fried, M; Major, C; Petrik, P, Imaging optical inspection device with a pinhole camera, EP2160591B1, NSZO: G01N21/8422, Europe

[2] G. Juhász, Z. Horváth, C. Major, P. Petrik, O. Polgár, M. Fried, Non-collimated beam ellipsometry, physica status solidi c Volume 5, Issue 5, p. 1081-1084, (2008) https://doi.org/10.1002/pssc.200777862

[3] C. Major, G. Juhasz, Z. Horvath, O. Polgar, M. Fried, "Wide angle beam ellipsometry for extremely large samples", Phys. Stat. Sol. (c), 5, Issue 5, p. 1077-1080 (2008) https://doi.org/10.1002/pssc.200777859

[4] C. Major, G. Juhasz, P. Petrik, Z. Horvath, O. Polgar, M. Fried, "Application of wide-angle beam spectroscopic ellipsometry for quality control in solar cell production", Vacuum 84, 119-122 (2009) https://doi.org/10.1016/j.vacuum.2009.05.013

[5] M. Fried, G. Juhasz, C. Major, P. Petrik, O. Polgar, Z. Horvath, A. Nutsch, "Expanded beam (macro-imaging) ellipsometry", Thin Solid Films 519, 2730-2736 (2011) https://doi.org/10.1016/j.tsf.2010.12.067

[6] A. Shan, M. Fried, G. Juhász, C. Major, O. Polgar, A. Nemeth, P. Petrik, L.R. Dahal, Jie Chen, Zhiquan Huang, N.J. Podraza, R.W. Collins "High Speed Imaging/Mapping Spectroscopic Ellipsometry for in Line Analysis of Roll to Roll Thin Film Photovoltaics", IEEE Journal of Photovoltaics, 4:(1) 355-361 (2014) DOI:10.1016/J.VACUUM.2009.05.013

[7] C. Major, G. Juhasz, Z. Labadi, M. Fried, "High speed spectroscopic ellipsometry technique for on-line monitoring in large area thin layer production," 2015 IEEE 42nd Photovoltaic Specialist Conference (PVSC), 2015, pp. 1-6, doi: 10.1109/PVSC.2015.7355640

[8] M. Fried, "On-line monitoring of solar cell module production by ellipsometry technique", Thin Solid Films, 571, 345-355 (2014) DOI:10.1016/j.tsf.2014.03.058

[9] P. Petrik, M. Fried, "Mapping and imaging of thin films on large surfaces", Physica Status Solidi (A) Applications and Materials Science, Open Access, v.219(13) July 2022, Article number 2100800 (2022) doi: 10.1002/pssa.202100800

[10] J. W. P. Bakker, H. Arwin, I. Lundström, and D. Filippini: Computer screen photoassisted off-null ellipsometry, Applied Optics Vol. 45, Issue 30, pp. 7795-7799 (2006) https://doi.org/10.1364/AO.45.007795

[11] Azzam R. M. A., Bashara N. M.: Ellipsometry and Polarized Light. Publisher: Elsevier North Holland, 1977, ISBN 0-7204-0694-3

[12] Hiroyuki Fujiwara: Spectroscopic Ellipsometry: Principles and Applications; Publisher: John Wiley & Sons, 2007: ISBN: 0470060182, 9780470060186

Contact angle determination by the Capillary Bridge Probe method: from perfect wetting to hydrophobic surfaces

N. Nagy[1*]

[1]*Institute of Technical Physics and Materials Science, Centre for Energy Research, P.O. Box 49, H-1525 Budapest, Hungary*

The developed indirect Capillary Bridge Probe method combines the accuracy of the Wilhelmy method and the general usability of the sessile drop method without their limitations. The method is based on the use of a liquid bridge as a probe: the capillary bridge of the test liquid is stretched between the base of a cylinder and the investigated surface under equilibrium conditions. The advancing contact angle on the sample can be measured during the stepwise or slow (quasi-static) decrease of the bridge length. The receding contact angle is determined during the retraction of the cylinder (Fig. 1).
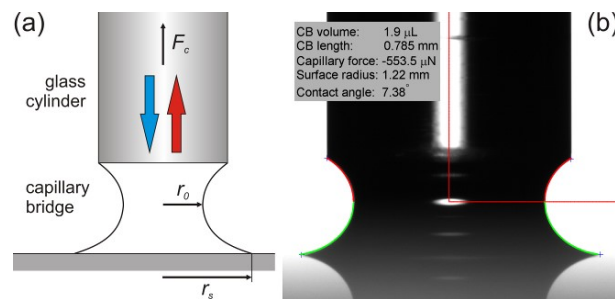
Figure 1. (a) *Schematics of a capillary bridge (F_c: capillary force; r_0: neck radius; r_s: contact line radius on the sample surface).* **(b)** *Captured and evaluated image of a water capillary bridge on a glass surface. The diameter of the glass cylinder is 2 mm. The blue crosses designate the corners of the bridge's silhouette, the red and green curves show calculated profile.*

The contact angle is calculated from Delaunay's analytical solution, while the three necessary parameters are the measured capillary force (F_c), the radius of neck or haunch (r_0), and the radius of the contact line (r_s) on the investigated surface. The latter two parameters are obtained from the automated analysis of the captured image of the liquid bridge. The radius of the upper contact line (r_c) is constant since it pins on the rim of the cylinder.
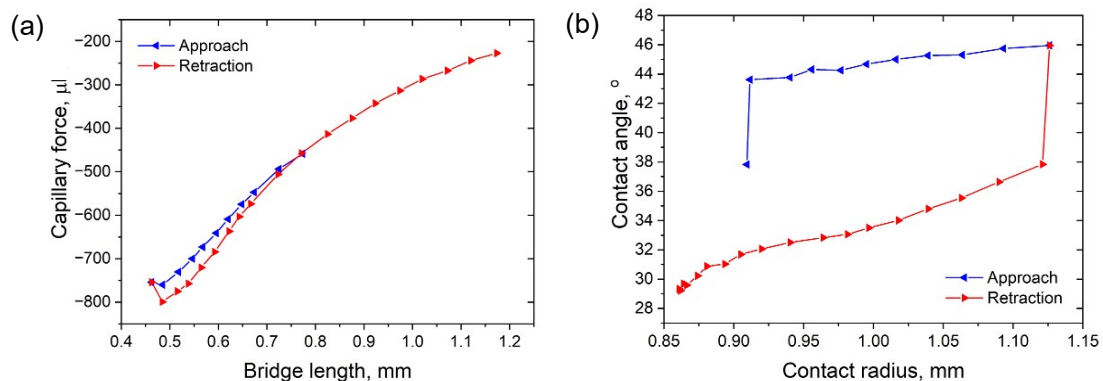
Figure 2. (a) *Capillary force as a function of bridge length measured on a hydrophilic Si_3N_4 surface.* **(b)** *Determined contact angles as a function of the contact radius. The force hysteresis results in contact angle hysteresis.*

A typical measured graph and determined contact angles are plotted in Fig. 2. The measurement was carried out on a clean stoichiometric Si_3N_4 surface. The attractive (negative) capillary force

decreases with the decreasing bridge length, and it shows hysteresis (Fig. 2(a)). This hysteresis results in the contact angle hysteresis in Fig. 2(b). The advancing contact angle is stable, while the receding values show decreasing character (similarly to the results of evaporating drop measurements).

As a demonstration of a unique property of the method, perfect wetting situations were also characterized. The graphs shown in Fig. 3 were measured on a superhydrophilic acid-treated glass surface. The capillary force and the contact angle do not exhibit hysteretic character. However, a novel phenomenon can be observed in Fig. 3(b). The contact line starts to advance again during the retraction and the corresponding (readvancing) contact angles are much lower than the advancing and receding values. In this phase, the readvancing contact line finds prewetted surface, this is the reason of the low determined values.
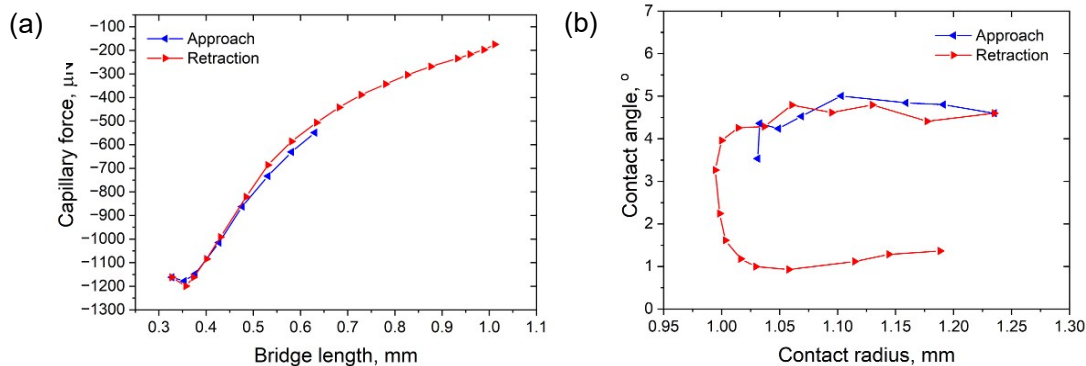
Figure 3. (a) *Capillary force as a function of bridge length measured on an acid-treated superhydrophilic glass surface.* **(b)** *Contact angles vs. the contact radius. The contact line starts to advance again during the retraction and the readvancing contact angles are much lower.*

Hydrophobic surfaces can be characterized with high sensitivity, as it was demonstrated on PTFE surfaces. The graphs in Fig. 4 show hysteresis of capillary force and contact angle, as well. Sessile drop measurements did not show any contact angle hysteresis.
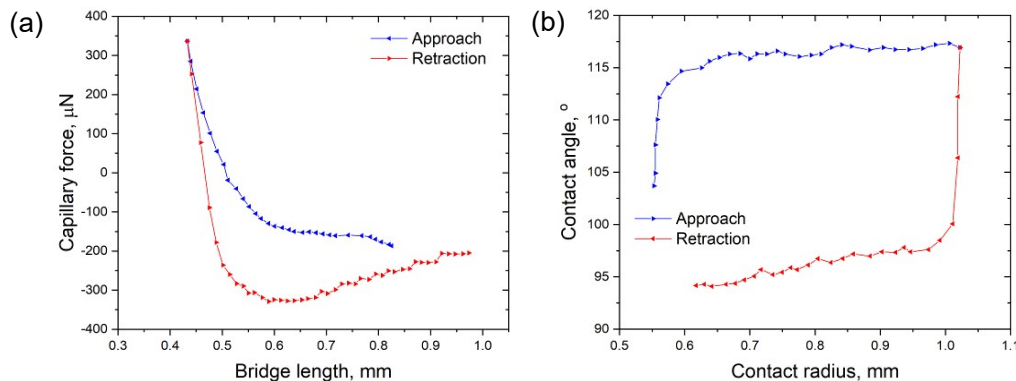
Figure 4. (a) *Capillary force vs. bridge length measured on a hydrophobic PTFE surface. The capillary force changes its sign during the approach and retraction.*
(b) *Contact angles as a function of the contact radius.*

References

[1] N. Nagy: Contact Angle Determination on Hydrophilic and Superhydrophilic Surfaces by Using r–θ-Type Capillary Bridges, *Langmuir* **35**, 2019, 5202-5212
[2] N. Nagy: Capillary Bridges on Hydrophobic Surfaces: Analytical Contact Angle Determination, *Langmuir* **38**, 2022, 6201-6208

Indentation size effect in exceptionally hard AlCu thin films

Dániel Olasz[1], György Sáfrán[1], Noémi Szász[1], Gabriella Huhn[2], Nguyen Quang Chinh[2]

[1]Eötvös Loránd Research Network, Center for Energy Research, Institute of Technical Physics and Materials Science, Thin Film Physics Laboratory, H-1121 Budapest, Konkoly-Thege M. St. 29-33, Hungary
[2] Department of Material Physics, Eötvös Loránd University, Pázmány Péter Sétány 1/A, Budapest, H-1117, Hungary

We investigated the correlations between the structure and mechanical properties of AlCu thin film system by efficient combinatorial methods: in one experiment, using DC magnetron sputtering, 10x1 mm, ~1.7 um thick thin films with discrete steps of varying composition (AlxCu1-x, $0 \leq x \leq 1$) were deposited on Si substrate in 15 adjacent bands representing the whole concentration range. The composition-dependent mechanical properties of the samples, such as their hardness, were determined by nanoindentation, and their composition and structure by microscopic methods (SEM, TEM) [1].
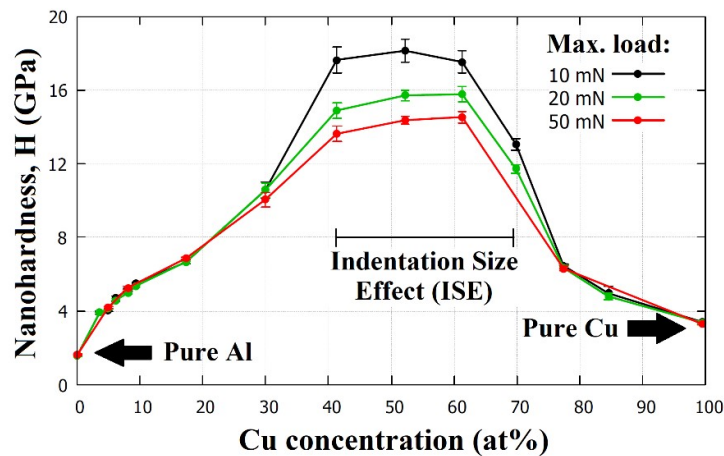
Figure 1: *Hardness of AlCu alloy thin films as a function of composition at maximum indentation forces of 10, 20 and 50 mN.*

Figure 1 shows the hardness (H) of the layers as a function of copper concentration. It can be observed that the hardness of pure Al (0 at% Cu) is 1.6 GPa, which is significantly higher than that of the bulk Al (~0.3 GPa). Even in the presence of a low alloying concentration of 3.7 at% Cu, the strength of the layer increases significantly to 3.9 GPa. The maximum strength value of ~16 GPa, which is 10 times harder than the pure Al thin film, is reached in the concentration range of ~40-60 at% Cu. This extraordinary strength is not only double the H=8 GPa [2] of the hardest AlCu thin film found in the literature but is also comparable to that of the materials used as hard coatings in the industry.

It can be observed in Figure 1 that at low alloying concentrations, the indentation measurements at 10, 20, 50 mN result in identical H values, while in the intermediate range ~40-70 at% Cu, lower maximum indentation forces are associated with higher H values. This phenomenon is known as the Indentation Size Effect (ISE), which is a well-known phenomenon for pure bulk Al and Cu materials. In contrast, our measurements showed the absence of ISE in the pure and low alloying concentration materials. The nanoindentation load-displacement (P-h) curves (Figure 2a) clearly show a step-like behavior in the ~40-70 at% Cu range, indicating a non-continuous deformation.

To gain a deeper understanding of the above phenomena, microstructural studies were carried out. Figure 2b shows a TEM image of the indented part of a lamella containing 52.2 at% Cu. The selected area electron diffraction (SAED) measurements showed the presence of Al_2Cu_3 and Al_4Cu_9 crystalline phases, with no Al(Cu) solid solution present at this composition. The image also shows that the layer is composed of narrow crystalline columns. In the figure, the arrows indicate the deformation bands formed by the indentation along which the crystalline columns were fractured. The high strength of the layers in the range of ~40-70 at% Cu composition, the pronounced precipitation character, the nanoscale grain structure and the presence of deformation bands are all indicative of a deformation mechanism typical of amorphous materials.
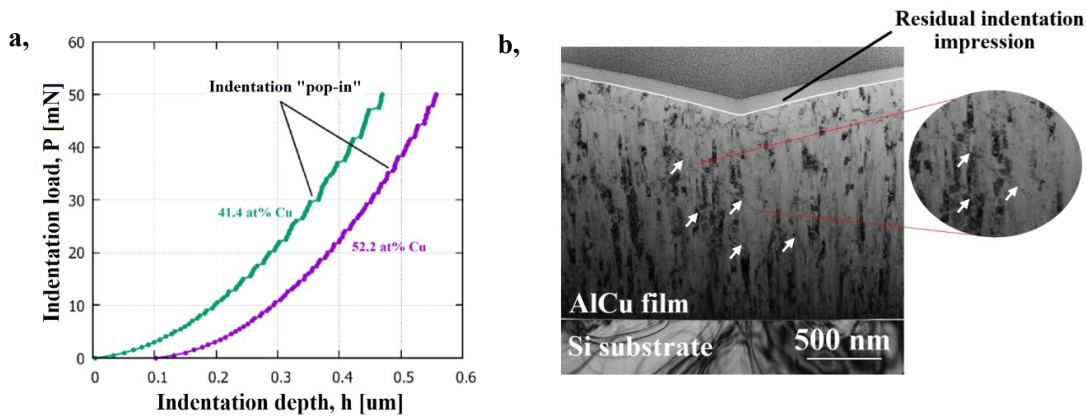
Figure 2: a, *"Step-like" indentation curves showing a "pop-in" phenomenon at a maximum indentation force of 50 mN.* **b,** *Cross-sectional TEM image of an indented layer containing 52.2 at% Cu. Arrows indicate the two deformation bands around the indentation.*

The absence of ISE at low alloying concentrations can also be explained by the microstructure. Even pure Al and Cu layers are characterised by very fine grain size (~ 100 nm), which increases the role of another deformation mechanism, the grain boundary sliding. AFM and SEM measurements confirm the increased activity of the grain boundary sliding mechanism, resulting in the formation of pile-ups around the indentation marks (Figure 3).
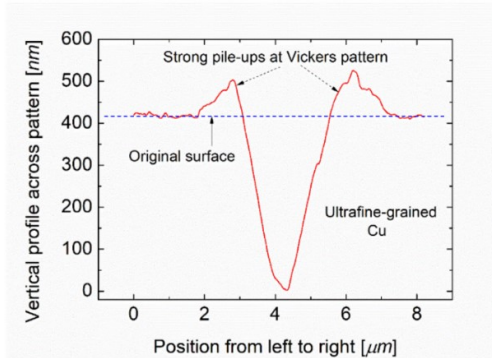
3. ábra: For a pure Cu layer, the vertical profile of the indentation trace determined by AFM. The "pile-up" phenomenon is clearly visible at the edge of the trace.

References:
[1] D.Olasz et al., Materials Letters 330, 133409, 2023
[2] M. Draissia et al., Phys. Scr. 69, 348, 2004

Detailing the problem of the analytical solution for the reflectivity of a double-layer coating deposited from different refractive indexes films

Tamás Kolonits[1] and Miklós Serényi[1*]

[1]*Institute for Technical Physics and Materials Science, Centre for Energy Research, Eötvös Loránd Research Network, Konkoly-Thege Miklós út 29-33, H-1121 Budapest, Hungary*

It is known for optical design that the two-layer antireflection coating can be planned with a simple, analytical calculation in the case of suitably chosen refractive indices. Solutions have been available since the 1940s and are discussed separately in textbooks. In this study, we present a solution to determine the parameter of a double layer coating using transfer matrices, and going further, we fully analyze the available residual reflection values for different refractive indexes. The efficiency of the double-layer design is illustrated by the application for a silicon detector operating in a narrow wavelength range.

Keywords: anti-reflection coatings, calculation

1. Introduction

In optics, optoelectronics and the semiconductor industry, the design of the anti-reflection layer is a very important application. Zero reflectivity can be achieved by applying a layer (or layer system) with appropriate refractive index (indices) and thickness (thicknesses). The reflectivity of a multi-layer system can be calculated by using the so-called transfer matrix (TM) method, introduced by Rouard [1]. Calculating the TM and the properties of a multi-layer system is complicated in general cases, therefore a number of numerical methods and special programs have been developed [2-7] that can optimize thin layer systems without user intervention. Analytical solutions typically use special restrictions of the refractive indices and/or the thicknesses of the layers candidate [8-11].

It is known that if the refractive index of a coating layer is less than that of the substrate, the reflectivity of their combination will be less than that of the substrate itself. The reflectivity has a minimum, if the optical thickness of the coating layer is quarter of the wavelength investigated. In one special case, when the refractive index of the coating layer is the square root of that of the substrate, the reflectivity is zero [8].

Searching in the manual, we find well-known, analytical solutions for the design of double layer anti-reflection layers. This, with suitably chosen refractive indices, results in effective but relatively narrow-band residual reflection. If we want to study the results of the design of double layer coatings more thoroughly, we must learning the so-called Schuster diagram [10]; the refractive index range where zero reflection can be reached is indicated here.

Although Schuster's activity concerns acoustics, he realized that his calculation technique is also suitable for the construction of optical spectral filters. For the theoretical treatment of the problems mentioned, the four-pole theory method known from high-frequency technology and acoustics was used advantageously.

The Schuster's paper discuss that, the ratio of the electrical and magnetic field components in a plane wave is to be considered the "optical characteristic impedance" of the relevant medium. This ratio formed within any plane wave process resulting from forwarding and a returning part should be generable spoken of as "optical resistance". The simplification of the computational handling of the problems that the four-pole theory contains is eventually based on the new formulation of the condition of continuity for the field components passing through an interface: the continuity conditions can be reduced to a continuity condition for the optical resistance.

22

It can be considered as belonging to the topic and used in the comparison of the layer arrangements an analytical solution of a special three-layer system. If the coating material with the special refractive index required by the substrate does not exist in technologically usable form, there is a possibility to construct a so-called equivalent system by forming a symmetrical three-layer structure of two coating materials [9-11]. In this case, the equivalent refractive index and equivalent optical thickness can be determined analytically, and a zero reflectivity can be achieved.

We find it worthwhile to dissect this topic further, because it is feared that Schuster's activity will become a thing of the past, as the use of computer numerical simulations is widespread. In this study, therefore, an analytical solution for minimizing the residual reflection of a double layer system is provided. It was found, if one of the coating materials has a refractive index smaller than the square root of that of the substrate and the other has a higher one, zero reflectivity could be achieved by a proper selection of the layer thicknesses. This result fully agrees with the message of Schuster diagram. In that case applying a double-layer system instead of a three-layer equivalent system is more efficient in time and costs.

2. Theoretical background

Let us to consider an electromagnetic (EM) wave with parallel polarization reaches an interface between the media "**0**" and "**1**". A part of the EM wave will be transmitted through; the other part will be reflected. The process could be described by the equation

$$\begin{pmatrix} E_1^+ \\ E_1^- \end{pmatrix} = \underline{\underline{M}} \begin{pmatrix} E_0^+ \\ E_0^- \end{pmatrix} \tag{1}$$

where E_0^+ is the part of the EM wave in medium "**0**" propagating into the positive direction; E_0^- propagates into the negative direction and so on. $\underline{\underline{M}}$ is the so-called *transfer matrix*} [12-15].

The elements of the transfer matrix $\underline{\underline{M}}$ are generally complex numbers and it is true that

$$M_{21}^* = M_{12} \text{ and } M_{22}^* = M_{11} \tag{2}$$

(where " * " refers to the complex conjugation), which is a consequence of the time reversal symmetry. In 1D approximation, the reflection amplitude is obtained from [12, 15]

$$r = -\frac{M_{21}}{M_{22}} \tag{3}$$

Therefore the reflectivity of the system is:

$$R = r \cdot r^* = \left| \frac{M_{21}}{M_{22}} \right|^2 = \frac{M_{21} \cdot M_{21}^*}{M_{22} \cdot M_{22}^*} = \frac{M_{21} \cdot M_{12}}{M_{22} \cdot M_{11}} \tag{4}$$

Using Epstein's notations [16], the transfer matrix of a system containing two thin layers on a substrate is:

$$\underline{\underline{M}} = \frac{1}{2} \begin{pmatrix} 1 & -1 \\ 1 & 1 \end{pmatrix} \underline{\underline{L_2}}(n_2, \beta) \underline{\underline{L_1}}(n_1, \alpha) \begin{pmatrix} 1 & 1 \\ -n_0 & n_0 \end{pmatrix} \tag{5}$$

assuming that the light propagates perpendicular to the surface, and the refractive index of the air is approximately 1. In Eq. (5) n_0 corresponds to the refractive index of the substrate and $\underline{\underline{L}}$ matrices represents the coating layers and defined as:

$$\underline{\underline{L_1}}(n_1, L_1) = \begin{pmatrix} \cos(kL_1) & \frac{1}{n_1}\sin(kL_1) \\ in_1\sin(kL_1) & \cos(kL_1) \end{pmatrix} = \begin{pmatrix} \cos\alpha & \frac{i}{n_1}\sin\alpha \\ in_1\sin\alpha & \cos\alpha \end{pmatrix} \tag{6}$$

where n_1 is the refractive index, L_1 the physical thickness and

$$\alpha = \frac{2\pi}{\lambda} n_1 L_1 \tag{7}$$

is the so-called "optical thickness" of the first coating layer [16] (λ is the wavelength of the light). $\underline{\underline{L_2}}$ corresponds to the second coating layer has a similar form.

3. Reflectivity of a double-layer system

Consider a system of two thin layers with optical thicknesses of α and β refractive indices of n_1 and n_2 on a substrate with a refractive index n_0. The light originates from vacuum/air, passes trough layers "**2**" and "**1**" and reaches the substrate. After calculating the transfer matrix defined in Eq. (5) and calculating it's reflectivity by Eq. (4), the reflectivity can be written as:

$$R = \frac{X - 2n_4}{X + 2n_4} \tag{8}$$

where

$$X = \left(n_0^2 + 1\right)\cos^2\alpha\cos^2\beta + \left(\frac{n_2^2}{n_1^2}n_0^2 + \frac{n_1^2}{n_2^2}\right)\sin^2\alpha\sin^2\beta + \left(\frac{n_0^2}{n_1^2} + n_1^2\right)\sin^2\alpha\cos^2\beta + \left(\frac{n_0^2}{n_2^2} + n_2^2\right)\cos^2\alpha\sin^2\beta$$
$$- 2\frac{(n_2^2-1)(n_0^2-n_1^2)}{n_1 n_2}\sin\alpha\cos\alpha\sin\beta\cos\beta \tag{9}$$

The problem to solve is finding the optical thicknesses α and β where the reflectivity has extrema (minima) as a function of the refractive indices n_0, n_1 and n_2.

3.1 Finding the minima of R

As a consequence of Eq. (8), the criterion of the minimal reflectivity is the zero gradient of X:

$$\underline{\nabla}R - \underline{0} \leftrightarrow \underline{\nabla}X - \underline{0} \tag{10}$$

3.2 Periodicity of the solution

By performing the partial derivations, Eq. (10) can be expressed as:

$$(B' - A'\cos 2\beta)\sin 2\alpha - 2\cos 2\alpha\sin 2\beta = 0 \leftrightarrow \tan 2\alpha = \frac{1}{2}\frac{\sin 2\beta}{B' - A'\cos 2\beta}$$
$$(D' - A'\cos 2\alpha)\sin 2\beta - 2\cos 2\beta\sin 2\alpha = 0 \leftrightarrow \tan 2\beta = \frac{1}{2}\frac{\sin 2\alpha}{D' - A'\cos 2\alpha} \tag{11}$$

where

$$A' = \frac{n_1^2 + n_2^2}{n_1 n_2} \quad B' = \frac{(n_1^2-n_0^2)(n_1^2-n_2^2)(n_2^2+1)}{n_1 n_2(n_0^2-n_1^2)(n_2^2-1)} \quad D' = -\frac{(n_0^2+n_1^2)(n_1^2-n_2^2)}{n_1 n_2(n_0^2-n_1^2)} \tag{12}$$

Eq. (11) has two consequences: first, all the solutions have a periodicity of π (both in α and β independently). Second, if (α_1, β_1) is a solution, also $(\pi - \alpha_1, \pi - \beta_1)$ will be one (the solution is centrally symmetric to $(\pi/2, \pi/2)$). These properties can be seen as an example on fig. 1. using coating with SiO$_2$ (silicon dioxide) and Ta$_2$O$_5$ (tantalum pentoxide) on a Si substrate.

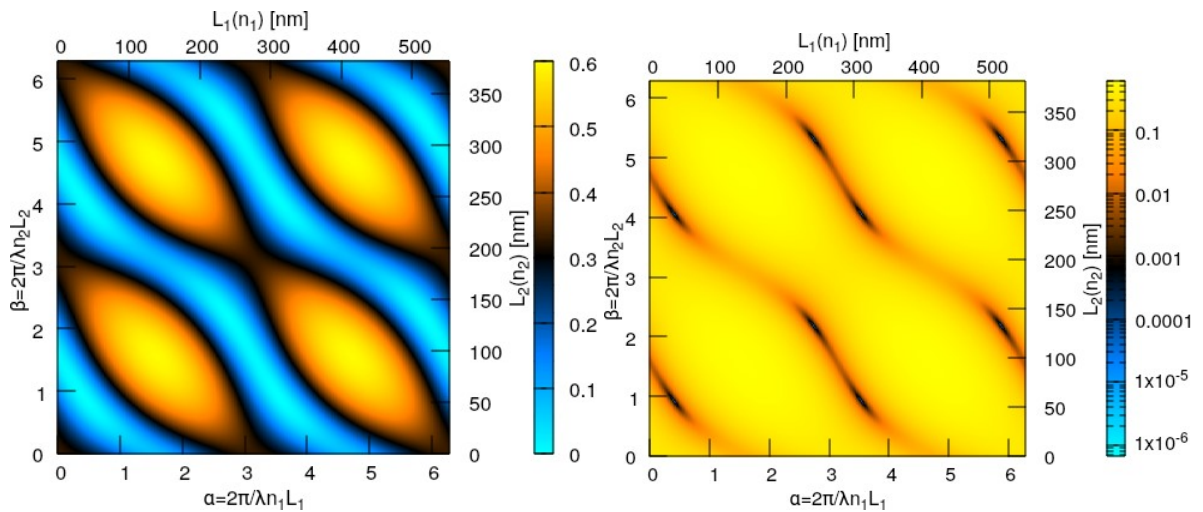
Fig. 1. Reflectivity of a double-layer system contains Si as substrate, SiO$_2$ as first layer and Ta$_2$O$_5$ as second one. The corresponding refractive indices are $n_0=3.7$, $n_1=1.45$ and $n_2=2.1$. Left: linear palette. Right: logarithmic palette. Optical and real thicknesses (at wavelength $\lambda=800$ nm) were both indicated.

3.3 Solving $\nabla X = 0$

Due to the consequences of Eq. (11) we could search the solution(s) in the interval $[0, \pi/2]$. In this interval, function $\sin^2$ is strictly monotonous; therefore we can obtain the partial derives on X as

$$\frac{\partial X}{\partial \sin^2 \alpha} \cdot \frac{\partial \sin^2 \alpha}{\partial \alpha} = [\ldots]_1 \cdot 2\sin\alpha\cos\alpha = 0$$
$$\frac{\partial X}{\partial \sin^2 \beta} \cdot \frac{\partial \sin^2 \beta}{\partial \beta} = [\ldots]_2 \cdot 2\sin\beta\cos\beta = 0 \tag{13}$$

It can be proven, that there are two sets of solutions: $\sin\alpha\cos\alpha = 0 \cap \sin\beta\cos\beta = 0$ or $[\ldots]_1 = 0 \cap [\ldots]_2 = 0$ (except very special cases of the refractive indices). Let's denote the four solutions of the first set as $\alpha_1 \ldots \alpha_4$ and $\beta_1 \ldots \beta_4$ respectively and call them the *trivial solutions*:

$$\sin\alpha_1 = 0 \sin\beta_1 = 0 \Rightarrow \alpha_1 = 0 \beta_1 = 0$$
$$\sin\alpha_2 = 1 \sin\beta_2 = 0 \Rightarrow \alpha_2 = \pi/2 \beta_2 = 0$$
$$\sin\alpha_3 = 0 \sin\beta_3 = 1 \Rightarrow \alpha_3 = 0 \beta_3 = \pi/2$$
$$\sin\alpha_4 = 1 \sin\beta_4 = 1 \Rightarrow \alpha_4 = \pi/2 \beta_4 = \pi/2 \tag{14}$$

(and the solutions are periodic with π).

Neglecting the trivial solutions $\sin\alpha\cos\alpha = 0$ and $\sin\beta\cos\beta = 0$ and introducing $x = \sin^2\alpha$ and $y = \sin^2\beta$ we got two equations:

$$A \cdot x + B - \sqrt{\frac{x-x^2}{y-y^2}} \cdot (1 - 2 \cdot y) = 0 \tag{15}$$

$$A \cdot y + D - \sqrt{\frac{y-y^2}{x-x^2}} \cdot (1 - 2 \cdot x) = 0 \tag{16}$$

where

$$A = \frac{n_1^2 + n_2^2}{n_1 n_2} \quad B = -\frac{n_1(n_0^2 - n_2^2)}{n_2(n_0^2 - n_1^2)} \quad D = -\frac{n_2(n_1^2 - 1)}{n_1(n_2^2 - 1)} \tag{17}$$

Equations (15) and (16) could be rewritten as

$$(Ax + B)(Ay + D) = (1 - 2y)(1 - 2x) \tag{18}$$

$$\frac{Ax + B}{Ay + D} = \frac{x - x^2}{y - y^2} \frac{1 - 2y}{1 - 2x} \tag{19}$$

which is a fourth order problem. From Eq. (18) we could express y as a function of x (or x as a function of y):

$$y = \frac{(1 - BD) - (AD + 2)x}{(AB + 2) + (A^2 - 4)x} \tag{20}$$

$$x = \frac{(1 - BD) - (AB + 2)y}{(AD + 2) + (A^2 - 4)y} \tag{21}$$

Substituting Eq. (20) back to Eq. (19) basically we got a fourth order equation. However this equation can be rearranged to the form

$$(1 - 2x)(Ax + B)\left\{(A + 2D)^2 - \frac{[1 - BD - (AD + 2)x] \cdot [AB + BD + 1 + (A^2 + AD - 2)x]}{x - x^2}\right\} = 0 \tag{22}$$

therefore we got two of the solutions by

$$1 - 2x_5 = 0 \Rightarrow \alpha_5 = +\frac{\pi}{4} + n \cdot \frac{\pi}{2} n \in \mathbb{Z} \tag{23}$$

$$Ax_6 + B = 0 \tag{24}$$

It should be noted, that using Eq. (21), solution defined by Eq. (24) can be rewritten as:

$$Ax_6 + B - \frac{(A + 2B)(1 - 3y_6)}{(AB + 2) + (A - 4)y_6} = 0 \tag{25}$$

therefore solution defined by Eq. (24) equals to

$$1 - 2y_6 = 0 \Rightarrow \beta_6 = \pm\frac{\pi}{4} + n \cdot \frac{\pi}{2} n \in \mathbb{Z} \tag{26}$$

The remaining solution(s) are defined by the second order part of Eq. (22). The general solution(s) with the refractive indices:

$$x_{7,8} = \frac{n_1^2[\pm n_0(n_1^2+1)-(n_0^2+n_2^2)]}{(n_0^2-n_1^2)(n_2^2-n_1^2)}$$

(27)

Remember, that x was defined as $sin^2\alpha$. It can be proven, that x_8 is never a true solution (i.e. never lays between 0 and 1), and there is also no guarantee x_7 (or the corresponding y_7) is a true solution (it depends on the current values of the refractive indices). Similar notes have to be taken on solutions defined by equations (23) and (26).

Positions, where the reflectivity has extremum are summarized in table 1. In this table the result of a numerical calculation in percentage in respect of the existing solution was also noted (based on 68921 cases, when n_0, n_1 and n_2 were uniformly distributed between 1 and 5).

Table 1. Positions, where the reflectivity has extremum. The first 4 solutions are the consequences of searching extremum of a periodic function on a restricted range and always exist. The second four are the solutions of the fourth order equation and not necessary describing a true $x = sin^2\alpha$ or $y = sin^2\beta$ value.

Position defined by		notes
$sin^2\alpha_1 = 0$	$sin^2\beta_1 = 0$	There are no layers
$sin^2\alpha_2 = 1$	$sin^2\beta_2 = 0$	So-called "lambda-quarter layer" [8]
$sin^2\alpha_3 = 0$	$sin^2\beta_3 = 1$	So-called "lambda-quarter layer" [8]
$sin^2\alpha_4 = 1$	$sin^2\beta_4 = 1$	So-called "double lambda-quarter" [8]
$x_5 = \dfrac{1}{2}$	$y_5 = \dfrac{(n_1^2-1)n_2^2}{(n_2^2-1)(n_1^2-n_2^2)}$	Exists in 81.86% of cases
$x_6 = \dfrac{(n_0^2-n_2^2)n_1^2}{(n_0^2-n_1^2)(n_1^2+n_2^2)}$	$y_6 = \dfrac{1}{2}$	Exists in 51.17% of cases
$x_7 = \dfrac{n_1^2[n_0(n_2^2+1)-(n_0^2+n_2^2)]}{(n_0^2-n_1^2)(n_2^2-n_1^2)}$	$y_7 = \dfrac{n_2^2[(n_0^2+n_1^2)-n_0(n_1^2+1)]}{(n_2^2-1)(n_2^2-n_1^2)n_0}$	Exists in 31.24% of cases
$x_8 = \dfrac{n_1^2[-n_0(n_2^2+1)-(n_0^2+n_2^2)]}{(n_0^2-n_1^2)(n_2^2-n_1^2)}$	$y_7 = \dfrac{n_2^2[-(n_0^2+n_1^2)-n_0(n_1^2+1)]}{(n_2^2-1)(n_2^2-n_1^2)n_0}$	Never exists between 0 and 1

3.4 Calculating the reflectivity regarding to the refractive indices

In Table 2 the values of the reflectivity as a function of refractive indices were summarized regarding to the positions defined by Table 1. Only the last row needs some explanation.

If we substitute back x_7 and y_7 into Eq. (9) the last term corresponds to $2\frac{(n_1^2-1)(n_0^2-n_2^2)}{n_1 n_2}sin\alpha cos\alpha sin\beta cos\beta$ will be:

$$2\frac{\sqrt{([n_0^2(n_1^2+1)(n_1^2+n_2^2)+n_2^2(n_0^2+n_1^2)^2]-[n_0(n_1^2+n_2^2)(n_1^2+1)(n_0^2+n_1^2)])^2}}{n_0(n_0^2-n_1^2)^2}$$

(28)

therefore the term below the root sign gains a ± depending on is $n_0^2(n_1^2+1)(n_1^2+n_2^4)+n_2^2(n_0^2+n_1^2)^2$ greater than $n_0(n_1^2+n_2^2)(n_2^2+1)(n_0^2+n_1^2)$ or not.

26

Table 2. Values the reflectivity in the extremum positions described in table 1.

Position defined by	reflectivity
$\sin^2 \alpha_1 = 0 \cap \sin^2 \beta_1 = 0$	$R_1 = \left(\dfrac{n_0 - 1}{n_0 + 1} \right)^2$
$\sin^2 \alpha_2 = 1 \cap \sin^2 \beta_2 = 0$	$R_2 = \left(\dfrac{n_0 - n_1^2}{n_0 + n_1^2} \right)^2$
$\sin^2 \alpha_3 = 0 \cap \sin^2 \beta_3 = 1$	$R_3 = \left(\dfrac{n_0 - n_2^2}{n_0 + n_2^2} \right)^2$
$\sin^2 \alpha_4 = 1 \cap \sin^2 \beta_4 = 1$	$R_4 = \left(\dfrac{n_1^2 - n_0 n_2^2}{n_1^2 + n_0 n_2^2} \right)^2$
$x_5 = \dfrac{1}{2} y_5 = \ldots$	$R_5 = \dfrac{\dfrac{(n_0^2 + n_1^2)(n_2^2 + 1)}{n_1^2 + n_2^2} - \dfrac{(n_0^2 - n_1^2)(n_1^2 - 1)}{(n_1^2 + n_2^2)n_1} \sqrt{\dfrac{n_1^4 - n_1^2}{n_1^2 - 1}} - 2n_0}{\dfrac{(n_0^2 + n_1^2)(n_2^2 + 1)}{n_1^2 + n_2^2} - \dfrac{(n_0^2 - n_1^2)(n_1^2 - 1)}{(n_1^2 + n_2^2)n_1} \sqrt{\dfrac{n_2^4 - n_1^2}{n_1^2 - 1}} + 2n_0}$
$x_6 = \ldots y_6 = \dfrac{1}{2}$	$R_6 = \dfrac{\dfrac{(n_0^2 + n_1^2)(n_2^2 + 1)}{n_1^2 + n_2^2} - \dfrac{(n_0^2 - n_2^2)(n_2^2 - 1)}{(n_1^2 + n_2^2)n_2} \sqrt{\dfrac{n_0^2 n_2^2 - n_1^4}{n_0^2 - n_2^2}} - 2n_0}{\dfrac{(n_0^2 + n_1^2)(n_2^2 + 1)}{n_1^2 + n_2^2} - \dfrac{(n_0^2 - n_2^2)(n_2^2 - 1)}{(n_1^2 + n_2^2)n_2} \sqrt{\dfrac{n_0^2 n_2^2 - n_1^4}{n_0^2 - n_2^2}} + 2n_0}$
$x_7 = \dfrac{n_1^2 [n_0(n_2^2 + 1) - (n_0^2 + n_2^2)]}{(n_0^2 - n_1^2)(n_2^2 - n_1^2)} y_7 = \ldots$	$R_7 = \begin{cases} \text{too long to display} \\ 0 \\ 4n_0 \end{cases}$

Therefore

$$X_7 = \frac{2}{(n_2^2 - n_1^2)^2} \left((1 \pm 1)(n_1^2 + n_2^2)(n_2^2 + 1)(n_0^2 + n_1^2) \mp n_0 \left[(n_1^2 + 1)(n_1^2 + n_2^4) \pm n_1^2 (n_2^2 + 1)^2 \right] - (1 \pm 1) \frac{n_1^2}{n_0}(n_0^2 - n_1^2)^2 \right) \quad (29)$$

viz.

$$X_7 - \begin{cases} \dfrac{2 \left(2(n_1^2 - n_2^2)(n_2^2 + 1)(n_0^2 + n_1^2) - n_0 \left[(n_1^2 + 1)(n_1^2 + n_2^4) + n_1^2(n_2^2 + 1)^2 \right] - 2\frac{n_1^2}{n_0}(n_0^2 + n_1^2)^2 \right)}{(n_2^2 - n_1^2)^2} \\ 2n_0 \end{cases} \quad (30)$$

Therefore, the reflectivity is:

$$R_7 = \begin{cases} \dfrac{2(n_1^2 + n_2^2)(n_2^2 + 1)(n_0^2 + n_1^2) - n_0 \left[(n_1^2 + 1)(n_1^2 + n_2^4) + n_1^2(n_2^2 + 1)^2 + (n_2^2 - n_1^2)^2 \right] - 2\frac{n_1^2}{n_0}(n_0^2 + n_1^2)^2}{2(n_1^2 + n_2^2)(n_2^2 + 1)(n_0^2 + n_1^2) - n_0 \left[(n_1^2 + 1)(n_1^2 + n_2^4) + n_1^2(n_2^2 + 1)^2 - (n_2^2 - n_1^2)^2 \right] - 2\frac{n_1^2}{n_0}(n_0^2 + n_1^2)^2} \\ 0 \end{cases} \quad (31)$$

That means, in certain cases, zero reflectivity can be achieved.

3.5 Numerical analysis of the result

In order to investigate, which extremum position form (α_1, β_1) to (α_7, β_7) describe the minimum (or maximum) reflectivity in a current combination of the refractive indices n_0, n_1 and n_2, 68921 cases were investigated, when n_0, n_1 and n_2 were uniformly distributed between 1 and 5. The results are the following:

The result of the calculations completely matches the result of Schuster's calculus and, of course, like his, it contains the simple analytical formulas that we know from textbooks.

- It was turned out, that in the entire cases one of the trivial solutions from (α_1, β_1) to (α_4, β_4) resulted the global maximum of the reflectivity. These solutions are well known in the literature [8] and called "lambda-quarter layer" or "double lambda-quarter layers".

- As it was mentioned above, the extremum positions described by (α_5, β_5) and (α_6, β_6) do not exist in every cases. Moreover, the reflectivity reaches the global minimum at these points only in very special cases (i.e. $n_1 = n_2$ or $n_0 = n_2$).

- In ~13% of the cases, solution defined by (α_7, β_7) existed, but was not the global minimum (the global minimum was one of the trivial solutions). These cases cannot be summarized with a few simple selection rules about the refractive indices n_0, n_1 and n_2.

- However, in every cases, when $n_1 \leq \sqrt{n_0} \cap n_2 \geq \sqrt{n_0}$ or $n_1 \geq \sqrt{n_0} \cap n_2 \leq \sqrt{n_0}$, the global minimum of the reflectivity was described by the point (α_7, β_7), and the reflectivity in this point was exactly 0.

4. Application example: silicon detector

Consider a silicon detector operating on the wavelength 800 nm as a substrate with a refractive index $n_0 = 3.7$. The first coating layer is SiO_2 with a refractive index $n_1 = 1.45$ which is significantly lower than the square root of n_0 ($\sqrt{3.7} \approx 1.92$). The second coating layer is Ta_2O_5 with a refractive index $n_2 = 2.1$. In this case, zero reflectivity can be achieved at the optical thicknesses of $(\alpha_7, \beta_7) = (0.39873, 0.94126)$. The summary of the real thicknesses of the coating layers is 92 nm. In contrast, the optical thicknesses of the Herpin's equvivalent three-layer system [17] are $(0.34044, 0.85690, 0.34044)$ with a total of 111 nm real thickness [18]. The reflectivity of the system with different coating thicknesses can be seen on fig. 2a. Reflectivity values in extremum positions $(\alpha_1, \beta_1) - (\alpha_7, \beta_7)$ are summarized in table 3.

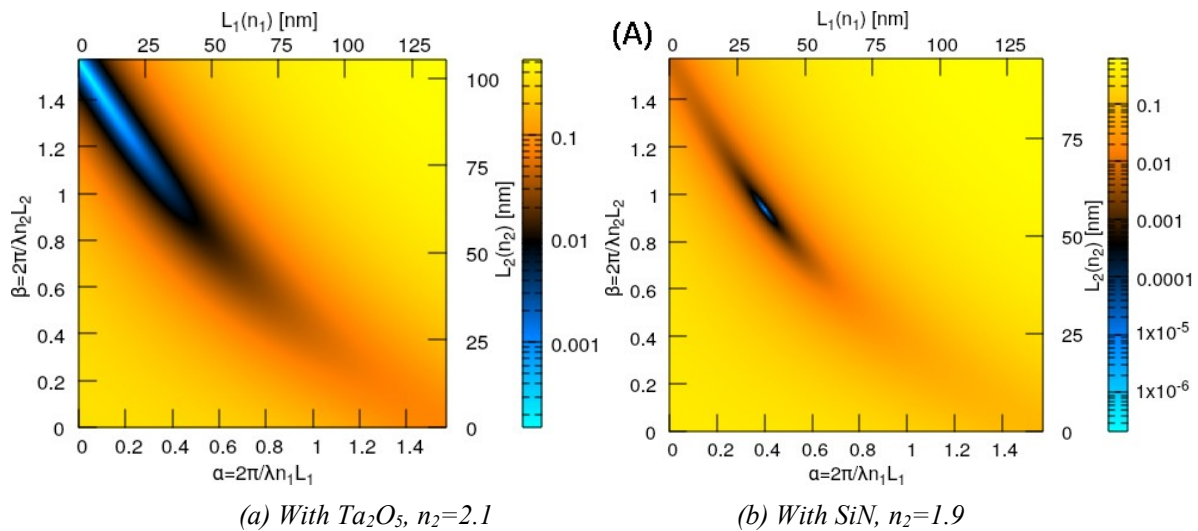*(a) With Ta$_2$O$_5$, n$_2$=2.1*   *(b) With SiN, n$_2$=1.9*

Fig. 2. Reflectivity of a double-layer system contains Si as substrate, SiO$_2$ as first layer and Ta$_2$O$_5$ or SiN as second one. Optical and real thicknesses (at wavelength λ=800 nm) were both indicated.

Table 3. Refractive indices and reflectivity values in positions $(\alpha_1, \beta_1) - (\alpha_7, \beta_7)$ of the example system Si as substrate, SiO_2 as first layer and Ta_2O_5 as second one. The corresponding refractive indices are $n_0=3.7$, $n_1=1.45$ and $n_2=2.1$. Optical and real thicknesses (at wavelength $\lambda=800$ nm) were both notated.

Solution	α	β	L_1 [nm]	L_2 [nm]	R
Trivial-1	0	0	0	0	0.3300
Trivial-2	$\pi/2$	0	138	0	0.0758
Trivial-3	0	$\pi/2$	0	95	0.0077
Trivial-4	$\pi/2$	$\pi/2$	138	95	0.5955
$x_5 = 1/2 \, y_5 = ...$	$\pi/4$	0.48692	69	30	0.0233
$x_6 = ... \, y_6 = 1/2$	0.53342	$\pi/4$	47	48	0.0025
$x_7 = ... \, y_7 = ...$	0.39873	0.94126	35	57	0

A counterexample, when the second coating layer is SiN with a refractive index $n_2=1.9$ which is just slightly smaller than $\sqrt{n_0} \approx 1.92$ can be seen on fig. 2b and in table 4. As it can be seen, the solution (α_7, β_7) does not exist in that case, and the minimal (but not zero) reflectivity is achieved applying only the second coating material with an optical thickness quarter of the wavelength.

Table 4. Refractive indices and reflectivity values in positions $(\alpha_1, \beta_1) - (\alpha_7, \beta_7)$ of the example system Si as substrate, SiO_2 as first layer and SiN as second one. The corresponding refractive indices are $n_0=3.7$, $n_1=1.45$ and $n_2=1.9$. Optical and real thicknesses (at wavelength $\lambda=800$ nm) were both notated.

Solution	α	β	L_1 [nm]	L_2 [nm]	R
Trivial-1	0	0	0	0	0.3300
Trivial-2	$\pi/2$	0	138	0	0.0758
Trivial-3	0	$\pi/2$	0	105	0.0002
Trivial-4	$\pi/2$	$\pi/2$	138	105	0.5300
$x_5 = 1/2 \, y_5 = ...$	$\pi/4$	0.48692	69	36	0.0320
$x_6 = ... \, y_6 = 1/2$	0.60145	$\pi/4$	53	53	0.0148
$x_7 = ... \, y_7 = ...$	-	-	-	-	-

5. Conclusions

In this work, an analytical solution for the design of double-layer coatings is provided, regarding to the given refractive indices of the available materials. The dependence of the reflectivity on the layer thicknesses was analyzed and the optimum for minimizing it was found in analytical form. The main conclusions of the analysis are the following:

1. If one of the coating materials has a refractive index smaller than the square root of that of the substrate and the other has a higher one, zero reflectivity can be achieved. It was also illustrated by an example of a silicon detector operating in a narrow wavelength range. It was found, that the total physical thickness of the zero reflectivity double-layer system is smaller than that of the Herpin's equivalent three-layer system.

2. The calculation returns the results for the lambda quarters and twice the lambda quarters layers known from the textbooks.

3. If both of the deposited layers have a refractive index higher or lower than the square root of the refractive index of the substrate, the optimal (but not zero) residual reflectivity could be achieved by applying a double or a single-layer system with optical thicknesses of the quarter of the wavelength. The choice between the double and the single-layer system depends on the current values of the refractive indices.

Nowadays, simulation programs make it easy to design the optical layer systems. The advantage of the analytical solution is that it reveals the combination of refractive indices that are essential for the choice of the material of the layers. These considerations can also be applied to the design of anti-reflective double-layer coatings on light emitting optoelectronic components such as LEDs, as well as Fabry-Perot laser diodes and VCSELs.

Funding

References

[1] P. Rouard, "Etudes des propriétés optiques des lames métalliques très minces," in Annales de Physique, vol. 11 (EDP Sciences, 1937), pp. 291–384.
[2] A. Luce, A. Mahdavi, F. Marquardt, and H. Wankerl, "Tmm-fast, a transfer matrix computation package for multilayer thin-film optimization: tutorial," J. Opt. Soc. Am. 39, 1007–1013 (2022).
[3] OptiLayer GmbH, "Optilayer," https://www.optilayer.com/productsand-services/optilayer
[4] Thin Film Center Inc, "Thin film center," https://www.thinfilmcenter.com/essential.php
[5] RP Photonics AG, "Rp coating," https://www.rp-photonics.com/coating.html
[6] Software Spectra Inc, "Tfcalc," http://www.sspectra.com/support/index.html
[7] Scientific Computing International, "Film wizard," https://sci/soft.com/product/film-wizard
[8] J. R. Meyer-Arendt, Introduction to classical and modern optics (Prentice Hall, Englewood Cliffs, N.J., 1995), chap. 12, 4th ed.
[9] M. C. Ohmer, "Design of three-layer equivalent films," J. Opt. Soc. Am. 68, 137–139 (1978).
[10] K. Schuster, "Anwendung der Vierpoltheorie auf die Probleme der optischen Reflexions-minderung, Reflexionsverstärkung und der Interferenzfilter,"Ann. Phys., 6th Ser. 4, 352 (1949)
[11] J. A. Dobrowolski and S. H. C. Piotrowski, "Refractive index as a variable in the numerical design of optical thin film systems," Appl. Opt. 21, 1502–1511 (1982).
[12] P. Pereyra and A. Robledo-Martinez, "On the equivalence of the summation and transfer-matrix methods in wave propagation through multilayers of lossless and lossy media," Eur. J. Phys. 30, 393–401 (2009).
[13] O. S. Heavens, "Optical properties of thin films," Reports on Prog. Phys. 23, 1–65 (1960).

[14] M. C. Troparevsky, A. S. Sabau, A. R. Lupini, and Z. Zhang, "Transfer-matrix formalism for the calculation of optical response in multilayer systems: from coherent to incoherent interference," Opt. Express 18, 24715–24721 (2010).

[15] P. Mello, P. Pereyra, and N. Kumar, "Macroscopic approach to multichannel disordered conductors," Annals Phys. 181, 290–317 (1988).

[16] L. I. Epstein, "The design of optical filters," J. Opt. Soc. Am. 42, 806–810 (1952).

[17] A. Herpin and N. J. Cabannes, "Optique electromagnétique—calcul du pouvior réflecteur dun systeme stratifie quelconque," Comptes Rendus Hebdomadaires Des Seances De L Acad. Des Sci. 225, 182–183 (1947).

[18] H. A. MacLeod and H. A. Macleod, Thin-Film Optical Filters (CRC Press, 2010), chap. 6, 4th ed.

In-situ study of nickel silicide formation in thin films

E. Dodony[1,2], I. Dódony[3], Gy. Sáfrán[1]

[1]Eötvös Loránd Research Network, Center for Energy Research, Institute of Technical Physics and Materials Science, Thin Film Physics Laboratory, H-1121 Budapest, Konkoly-Thege M. St. 29-33, Hungary
[2] Department of Material Physics, Eötvös Loránd University, Pázmány Péter Sétány 1/A, Budapest, H-1117, Hungary
[3] NANOLAB, Research Institute of Biomolecular and Chemical Engineering, University of Pannonia, Veszprém, H-8201, Hungary
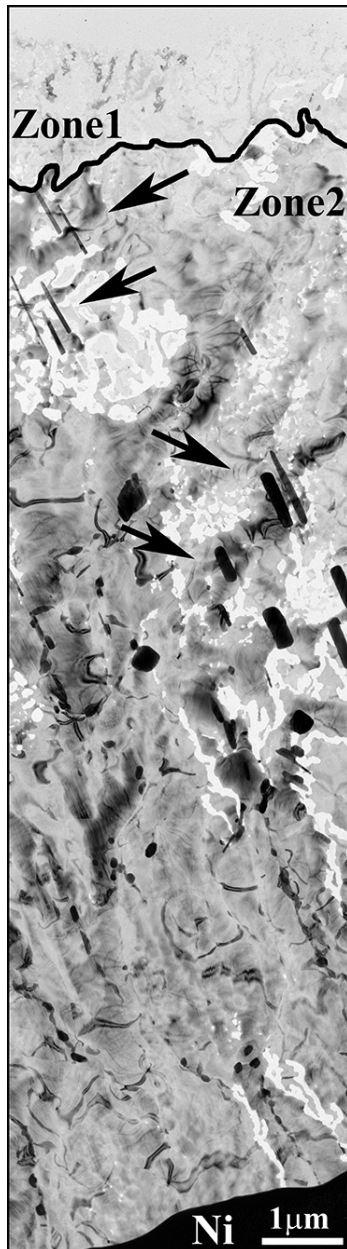
Figure 1 Bright field TEM image depicts reaction Zone 1 and 2 formed as a result of solid state reaction between Ni grid and a-Si layer. Arrows show whiskers protruding from the thin layer.

Due to their excellent physical and electrical properties nickel silicide layers have become one of the most promising components of microelectronics devices. To date, the mechanisms and reaction pathways of Ni-silicide formation remain unexplored, as the outcome depends on a wide range of experimental parameters (temperature, layer thickness, microstructure etc.). [i, ii, iii].

We studied in- and ex-situ the formation of nickel-silicides below 1073K in the solid state reactions between thin amorphous silicon (*a*-Si) layers and the supporting nickel TEM micro-grids. This unique experimental setup allowed us to reveal the sequentially forming phases of nickel-silicides, in lateral arrangement, by high resolution TEM (HRTEM) and selected area electron diffraction (SAED).

During heat treatments at 860K and 973K we identified, almost all known silicide phases in reaction Zone 1 and 2 shown by Fig.1 together with the Ni grid-bar at the lower right corner. The first reaction product observed was α-NiSi2, that was continuously present in Zone 1, at the reaction front advancing in the a-Si layer. (Fig.1). The HRTEM image in Fig.2(a) shows α-$NiSi_2$ in [110] orientation. Planar defects - stacking faults and micro-twins- are recognized both in the image and in the Fourier transform inset. While the average width of zone 1 remained constant, the width of zone 2 increased continuously during the reaction. Zone 2 is dominated by $Ni_{31}Si_{12}$. Fig.2 represents HRTEM image of [100] oriented γ-$Ni_{31}Si_{12}$ full of planar defects. Besides $Ni_{31}Si_{12}$ we identified further phases in Zone 2. They followed a tendency of increasing Ni content towards the Ni-grid bar as follows: NiSi, ε-Ni_3Si_2, δ-Ni_2Si, β_1-Ni_3Si, β_2-Ni_3Si. Together with these phases of Zone 2, the $Ni_{31}Si_{12}$ phase was abundant.

During the heat treatment elongated protrusions, whiskers (shown by arrows in Fig.2) were ejected preceded by an intense diffraction contrast change in the parent crystal, suggesting the accumulation of compressive stress. It was found that whisker and its parent grain consist of the same phase. As the reaction progresses and the parent grain transforms into a phase with a higher Ni concentration, whisker undergoes the same transformation (NiSi $\rightarrow$ Ni_3Si_2 $\rightarrow$ Ni_2Si $\rightarrow$ Ni_3Si). This explains the coexistence of whiskers of different phases. It is to mention that whisker

32

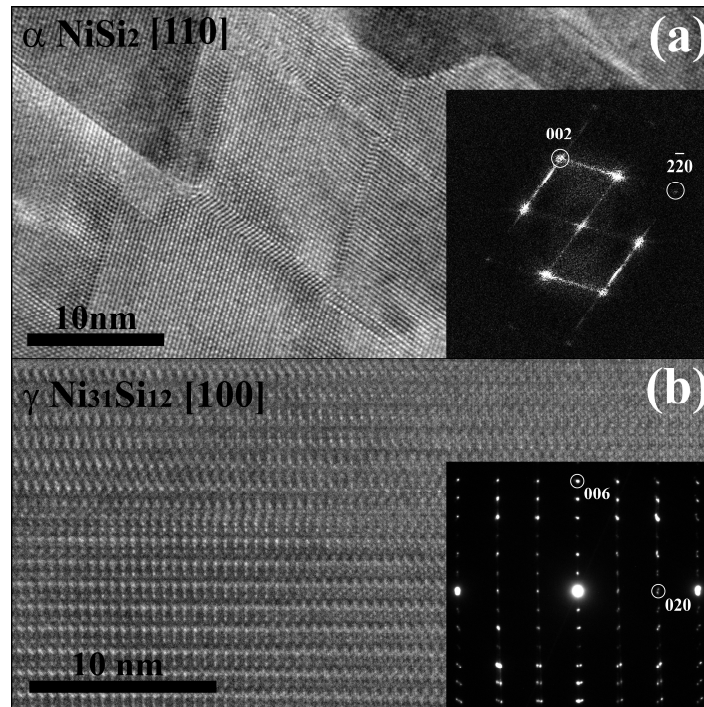formation in the solid-state reaction of Ni and Si was first observed in our experiments.

Figure 2 HRTEM image of (a) NiSi2, the typical phase of Zone 1, showing planar defects, stacking faults and micro twins depicted by the image and the FFT inset, (b) the dominant γ-($Ni_{31}Si_{12}$) phase of Zone 2 and its SEAD showing [100] orientation.

In conclusion, because of their excellent physical and chemical properties, phase variability, as well as their applicability in microelectronics, the present results on Ni-silicide could be of both scientific and technological importance. However, to get a complete picture of the formation of silicides as thin films and whiskers in the Ni-Si system, further detailed studies are needed.

[i] S. H. Chen, C., Carter, Z. Elgat, L R, Zheng, and J. W. Mayer, The structure of Ni5Si2 formed in Ni-Si thin film lateral diffusion couples, J. Appl. Phys. 62 (4), (1987) 1189-1194.

[ii] B. Bokhonov and M. Korchagin, In-situ investigation of the formation of nickel silicides during interaction of single-crystalline and amorphous silicon with nickel, Journal of Alloys and Compounds 319 (2001) 187–195.

[iii] F. Nemouchi, D. Mangelinck, J.L. Lábár, M. Putero, C. Bergman and P. Gas, A comparative study of nickel silicides and nickel germanides: Phase formation and kinetics, Microelectronic Engineering 83, 2006, 2101–2106.